Gap Winds and Wakes: SAR Observations and Numerical Simulations

FEIFEI PAN* AND RONALD B. SMITH

Department of Geology and Geophysics, Yale University, New Haven, Connecticut

(Manuscript received 9 September 1997, in final form 18 May 1998)

ABSTRACT

The nature of terrain-induced gap winds and wakes in the atmosphere is examined using surface wind data from synthetic aperture radar (SAR) and the shallow water equations. The shallow water model is used to predict the types of wake–jet wind patterns that might occur behind an idealized pair of bell-shaped hills with a gap between them. A regime diagram is constructed based on the width of the gap and the upstream Froude number. Specific predictions of the model are found to compare moderately well with SAR data from four examples of airflow near Unimak Island in the Aleutian Chain. The model predicts the observed wakes and jets, including jets that exceed the upstream speed. Theoretical analysis considers the relative importance of rising terrain and narrowing valley walls in the acceleration of gap winds. Wind speeds in the wake region are controlled by the Bernoulli function and regional pressure. Gap winds therefore are streams of air that have avoided Bernoulli loss over the terrain by passing through gaps. The speed of gap winds can exceed the upstream speed only in ridgelike situations when the regional leeside pressure is lower than the upstream pressure.

1. Introduction

a. Observations

The goal of this paper is to understand low-level gap winds and wakes generated by complex terrain. Gap winds are defined as jets of air, faster than adjacent airstreams, which occur downstream of gaps in an irregular mountain range. Wakes are regions of slower air in the lee of high terrain.

Although the theory of mountain airflow disturbance has advanced significantly over the last four decades (see section 1a), the ability to observe natural 3D atmospheric airflow patterns such as jets and wakes has progressed more slowly. Wakes have been detected in cloud patterns (Chopra 1973; Thomson et al. 1977; Etling 1989), but the relationship between cloud density and wind velocity is unclear. Satellite sunglint wake patterns have been reported by several authors (e.g., Smith et al. 1997) but these observations are not quantitative. Combined satellite and aircraft analyses of wakes are given by Smith and Grubišić (1993) and Smith et al. (1997). Several observational studies of gap winds have appeared (Table 1), but these have mostly used conventional surface data, balloon soundings, and aircraft data. Passive satellite remote sensing systems have also been used for gap wind studies (e.g., Clarke 1988; Fett 1993).

The recent development of active satellite-borne synthetic aperture radar (SAR) and scatterometer has greatly advanced our ability to measure the state of the sea and corresponding wind speed patterns over wide areas. Unlike sunglint, these technologies are global, all-weather (i.e., cloud penetrating), 24-h, and quantitative. The fact that this method of wind detection applies only to the ocean surface is not a fatal disadvantage for terrain airflow studies, as many of the simplest prototype terrain problems require an isolated topographic feature with flat surroundings. In this study, we used *ERS-1* SAR imagery of airflow near oceanic islands to verify the predictions of a "shallow water" model of airflow dynamics, probably the simplest model that captures the basic mechanisms of wake and jet formation.

b. Theories of gap winds and wakes

The two leading analytical models of mesoscale mountain airflow are the linear theory of continuously stratified flow and the nonlinear shallow water system (i.e., "hydraulic" theory). Full numerical simulations, including continuous stratification and nonlinearity, are also widely used. In the two sections below, we review the application of these analytical models to the gap flow problem.

* Current affiliation: School of Civil and Environmental Engineering, Georgia Institute of Technology, Atlanta, Georgia.

Corresponding author address: Ronald B. Smith, Department of Geology and Geophysics, Yale University, P.O. Box 208109, New Haven, CT 06520-8109.
E-mail: ronald.smith@yale.edu

TABLE 1. Gap wind observations.

Name/Region	Direction/Width	Reference
Tehuantepec, Mexico	NE/30 km	Hurd (1929), Stumpf (1975), Clarke (1988)
Bora, Croatia	NE/30 km	Smith (1987)
Hawaii	E/10 km	Smith and Grubisic' (1993)
St. Vincent, Caribbean	E/5 km	Smith et al. (1997)
Wyoming corridor	W/50 km	Marwitz and Dawson (1984)
Mistral, France	N/100 km	Pettre (1982), Jansa (1987), McAneny et al.(1988), Kaufmann and Weber (1996)
Ebro Valley, France/Spain	N/50 km	Masson and Bougeault (1996)
Taku, Alaska	NE/20 km	Colman and Dierking (1992)
Stampede Pass, Cascades	E/20 km	Reed (1981), Mass and Albright (1985), Colle and Mass (1998)
Fraser River, B.C.	NE/30 km	Mass et al. (1995)
Shikoko Island, Japan	S/30 km	Saito (1992, 1993)
Strait of Juan de Fuca, B.C.	E/30 km	Reed (1931), Colle and Mass (1996)
Strait of Gibraltar	W,E/20 km	Scorer (1952)
Howe Sound, B.C.	NNE/10 km	Finnigan et al. (1994), Jackson and Steyn (1994 a,b)
Kamishak Bay, Alaska	NW/30 km	Macklin et al. (1990), Fett (1993)
Shelikof Strait, Alaska	NE/50 km	Macklin et al. (1984), Lackmann and Overland (1989)
Western Ghats, India	W/30 km	Ramachandran et al. (1980)
Wide Bay, Alaska	NW/80 km	Bond and Macklin (1992)
Unimak Island, Alaska	N,S/15, 40 km	Present work

1) LINEAR THEORY WITH CONTINUOUS STRATIFICATION

According to the linear 2D theory of Queney (1948) for an unstructured atmosphere (i.e., constant stability and wind speed) and Klemp and Lilly (1975) for a structured atmosphere, steady vertically propagating mountain waves will produce accelerated winds on the lee slopes. These speed anomalies are proportional to the height of the ridge crest. To consider whether this result helps to understand gap winds and wakes, imagine a flow parallel to the x axis across a ridge aligned with the y axis, with slow modulations of the ridge height along its length (Saito 1993). If these modulations are smooth enough, the flow at each y position might behave in a locally two-dimensional fashion; that is, horizontal confluence and difluence could be neglected. This conceptual model leads us to the conclusion that the strongest winds would be downstream of the highest peaks along the ridge, the opposite of a gap jet.

To avoid the assumption of slow modulation (i.e., gentle ridgeline variation) and negligible confluence, we can examine the fully 3D linear solutions of Smith (1980, hereafter S80) for an incoming flow with a constant buoyancy frequency N and wind speed U_∞. By reason of linearity, we can superpose two of S80's bell shape hills:

$$h(x, y) = \frac{h_0}{(1 + x^2/a^2 + (y - y_1)^2/a^2)^{3/2}} + \frac{h_0}{(1 + x^2/a^2 + (y - y_2)^2/a^2)^{3/2}}, \quad (1)$$

where h_0 and a are the mountain heights and horizontal scales, respectively, and $(0, y_1)$ and $(0, y_2)$ are the positions of the two peaks. The surface pressure perturbation field can be expressed by

$$p'(x, y, o) = -\rho_0 N U_\infty h_0(x/a)\left[\frac{1}{(1 + x^2/a^2 + (y - y_1)^2/a^2)^{3/2}} + \frac{1}{(1 + x^2/a^2 + (y - y_2)^2/a^2)^{3/2}}\right]. \quad (2)$$

From (2) the wind speed anomoly can be derived using the linearized Bernoulli equation

$$u' = -(U_\infty \rho_0)^{-1} p' \quad (3)$$

from S80.

Figure 1 shows the surface pressure field calculated from (2), indicating that low pressure, and corresponding fast flow (3), is found only on the lee slopes. There is no strong pressure gradient along the gap axis and no strong gap wind (see also Blumen and Dietze 1981). This is so despite the fact that the solutions of S80 include significant horizontal confluence in the gaps. We conclude that the linear model with a radiation condition cannot predict gap winds. It is also apparent from this argument that linear theory does not predict wakes behind the highest peaks.

2) HYDRAULIC THEORIES

The hydraulic or layered models of mountain airflow were advanced in the context of one-dimensional flow by Long (1954) and Houghton and Kasahara (1968), and reviewed recently by Baines (1995) and others. Long showed that with a subcritical upstream Froude number $F_\infty < 1$, transition to supercritical flow (i.e., $F > 1$) will occur for a nondimensional ridge height ($M = h_0/H_\infty$) greater than

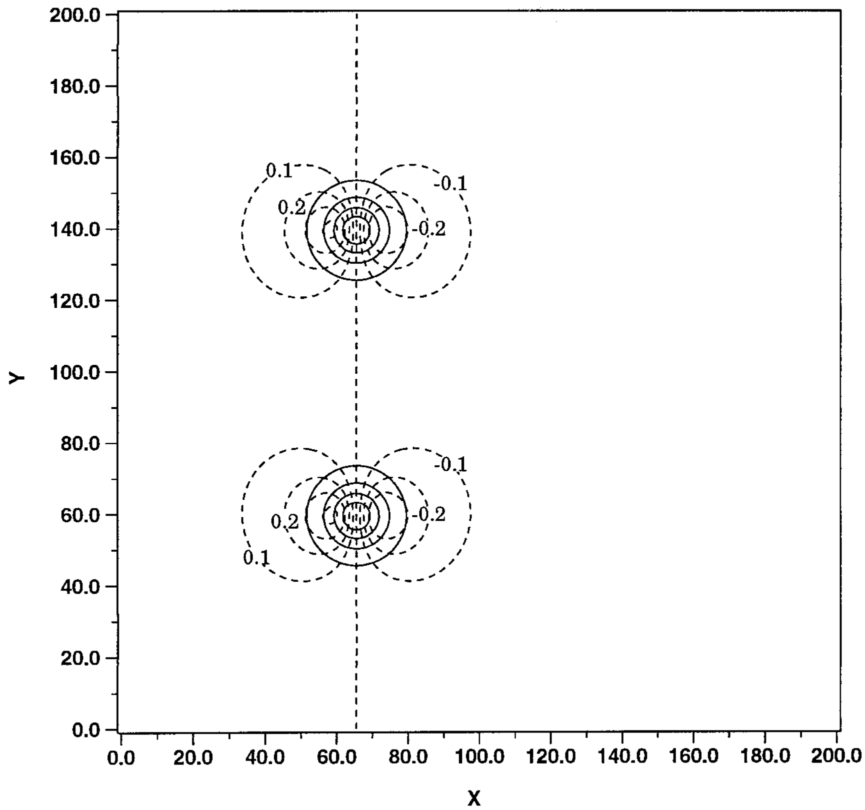

FIG. 1. The topographic contours of the two bell-shaped mountains given by Eq. (1) (shown in solid lines) and the isobars of perturbation surface pressure given by Eq. (2) (shown dashed). The airflow is from left to right.

$$M_c = 1 + \frac{1}{2}F_\infty^2 - \frac{3}{2}F_\infty^{2/3}, \tag{4}$$

where $F_\infty = U_\infty/\sqrt{g'H_\infty}$.

Arakawa (1969) extended Long's result by confining the flow in a channel with vertical walls, whose width varies as the terrain rises. The ratio of local channel width to its upstream value is denoted by D. Values of $D > 1$ ($D < 1$) indicate horizontal difluence (confluence). A subcritical flow can be brought to a critical state with a combination of rising terrain and narrowing channel (M_c, D_c) according to

$$M_c = 1 + \frac{1}{2}F_\infty^2 - \frac{3}{2}\left(\frac{F_\infty}{D_c}\right)^{2/3}. \tag{5}$$

These steady-state one-dimensional models have significantly contributed to our understanding of nonlinear flows, but they have the disadvantage of exhibiting certain singularities and an inability to represent two-dimensional features such as wakes, eddies, and gap and corner flows.

The starting point for our investigation is the recent work on 2D wake flows in one-layer models (Schär and Smith 1993a,b, henceforth SS93; Grubišić et al. 1995; Smith and Smith 1995; Smith et al. 1997). The correspondence between the one-layer model and continuous models has been discussed in several papers (Smith 1989; Schär 1993; Schär and Durran 1997; Smith et al. 1997). The one-layer studies indicate that hills accelerate the flow over the lee slopes but this acceleration leads to hydraulic jumps that dissipate energy and cause slower wake flows farther downstream. The stronger the local downslope Froude number, the greater the Bernoulli loss in the jumps and the weaker the flow in the wake. The current paper extends this type of model to more complex terrain situations. Other views of wake formation, such as the nondissipative vortex tilting conceptualization of Smolarkiewicz and Rotunno (1989), do not relate to the methods pursued here for wake and jet studies. The one-layer theory of corner winds, using the concept of a supercritical expansion fan (Samelson 1992; Samelson and Lentz 1994), is related to the current approach except that only supercritical flows with vertical walls were considered.

One goal of this paper is to test the hypothesis that gap winds are airstreams that have transitioned from subcritical to supercritical flow by passing over terrain and/or through a gap. Another issue in our investigation is the role of horizontal confluence of airflow through a gap. We are interested in the relative importance of rising terrain and narrowing valley walls in accelerating the flow toward a critical state. If the effect of confluence is large, gaps might generate critical flow before a high mountain would. In real terrain with sloping hillsides, it is difficult to predict in advance the role of confluence. We will compute the difluence factor D_c from the numerical solutions as a diagnostic quantity using (5).

The final element of our analysis is the role of the Bernoulli equation. Far downstream of the terrain, the pressure field may tend to equilibrate, so that jets and wakes will be controlled entirely by the Bernoulli losses, which occurred on each streamline as the fluid passed over the terrain. Equivalently, the potential vorticity generated over the terrain will be conserved downstream, controlling the downstream wakes and jets once balanced flow has been reestablished (SS93). These related concepts of Bernoulli loss and PV generation provide a simple link between processes over complex terrain and balanced flow far downstream.

In this article, we first investigate the mechanism of gap winds theoretically and numerically, using a one-layer shallow water model (SWM) to simulate jets through a gap formed by two bell-shaped hills. Later, we validate the SWM by comparing its predictions with observations from *ERS-1* SAR imagery from Unimak Island.

The arrangement of this paper is as follows. Section 2 describes the dynamics of gap flows predicted by the SWM with idealized two-hill terrain. Section 3 contains information about Unimak island. Section 4 introduces *ERS-1* SAR imagery and SAR image processing. Section 5 compares SWM results and observations from SAR imagery. Section 6 considers the role of the Bernoulli function in determining the wind speed. Section 7 is a summary.

2. Numerical simulations

a. The shallow water model (SWM)

We used a shallow water model developed by Schär and Smith (1993a,b) to represent airflow in the lower troposphere. A further description of this model can be found in Smith and Smith (1995), Grubišić et al. (1995), and Schär and Smolarkiewicz (1996). This model is based on the inviscid shallow water equations:

$$\frac{Du}{Dt} + \frac{\partial(h + H)}{\partial x} = 0, \tag{6}$$

$$\frac{\partial v}{Dt} + \frac{\partial(h + H)}{\partial y} = 0, \tag{7}$$

$$\frac{\partial H}{\partial t} + \frac{\partial(uH)}{\partial x} + \frac{\partial(vH)}{\partial y} = 0, \tag{8}$$

where u, v, h, and H are the nondimensional velocity components, the terrain height, and the fluid layer depth, respectively. The velocity components are scaled with the wave speed $\sqrt{g'H_\infty}$, whereas the terrain height and layer depth are scaled with H_∞. Dissipation in jumps is handled by proper treatment of mass and momentum conservation in the numerical scheme.

The nature of steady solutions to the shallow water equations depends on two nondimensional numbers: the upstream Froude number $F = U_\infty/\sqrt{g'H_\infty}$ (where U_∞ is the upstream flow speed, g' is the reduced gravity, and H_∞ is the upstream flow depth) and $M = h_0/H_\infty$ is the nondimensional mountain height (where h_0 is summit height of the obstacle). As there is no natural horizontal length scale in these equations, the solutions are scale invariant. For example, doubling all horizontal terrain scales leaves the flow stretched but unchanged. However, any number of length ratios may enter the problem to describe geometrical aspects of the terrain.

b. The choice of idealized terrain

An obvious choice for a family of idealized terrains in our theoretical studies would be an infinite ridge with a set of gaps of different widths and heights. One problem with this choice is that the infinite ridge promotes upstream blocking under certain conditions. To avoid this problem, we selected a ‘‘two-hill’’ family of terrains, given by (1). Any upstream blocking effect caused by this terrain disperses before reaching the domain boundary. One advantage of this choice is that the regime diagram for the ‘‘one-hill’’ version of this terrain (i.e., $y_1 = y_2$) has already been described by SS93. Another advantage is that it approximates the type of terrain found in our field area, Unimak Island, and elsewhere in the world where pairs of nearby volcanic peaks form airflow gaps (e.g., Hawaii, eastern Caribbean). By limiting our analysis to this family, however, we leave unexplored a wide variety of other interesting terrain configurations.

For the two-hill terrain, the gap width relative to the hill width is an important control parameter. From (1), we define the gap width $d = |y_1 - y_2|$ and the nondimensional gap width $G = d/a$. The nondimensional peak and gap heights are then, using (1)

$$M_1 = \frac{h(0, y_1)}{H_\infty} \approx \frac{h_0}{H_\infty}(1 + G^{-3}) \approx \frac{h_0}{H_\infty} \quad \text{for } G \gg 1 \tag{9}$$

and

$$M_2 = \frac{h(0, 0)}{H_\infty} = \frac{2h_0}{H_\infty}(1 + G^2/4)^{-3/2}. \tag{10}$$

c. Classification of flow past two hills

For a single isolated hill, flows with subcritical upstream conditions can be classified into two regimes: cases that remain subcritical everywhere and cases that develop critical flow over the terrain peak with super-

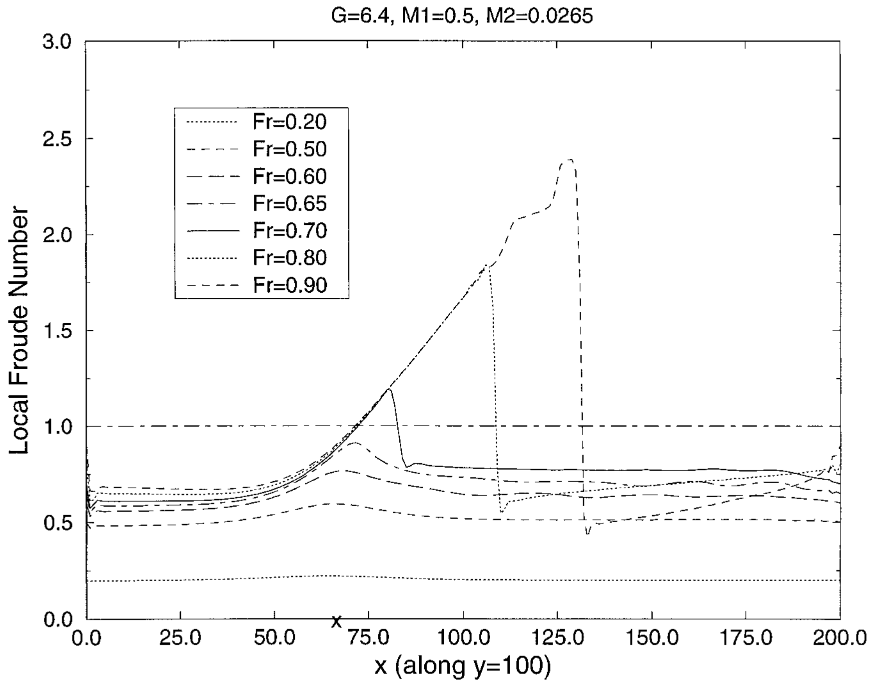

FIG. 2. Profiles of local Froude number along the gap axis for a mountain range with two peaks. The nondimensional mountain height is $h_0/H_\infty = 0.5$. The nondimensional gap width is 6.4. Seven calculations with different upstream Froude numbers are shown. The gap summit is located at $X = 65$. Upstream Froude numbers are labeled on the figure. Ambient Froude numbers 0.7 and higher give critical flow in the gap.

critical flow and jumps over the lee slopes (SS93). These latter cases exhibit wakes with reduced Bernoulli value, flanked by banners of potential vorticity.

With two hills instead of one, we must monitor the occurrence of critical flow over the peaks and in the gaps. This consideration gives rise to three classes instead of two:

class A: subcritical flow everywhere;
class B: critical flow over the peaks, with wakes downstream of the peaks;
class C: critical flow over the peaks and the gaps.

Note that this classification scheme presupposes that as higher terrain and higher upstream Froude numbers are considered, critical flow will occur first at the peaks, rather than the gaps. The validity of this assumption is not self-evident as confluence into the gaps might promote critical flow there, according to (5). However, our results indicate that the effect of confluence is not dominant, and thus the three classes A, B, and C are sufficient.

To investigate the onset of critical conditions, a set of numerical calculations were carried out with four gap widths (i.e., $G = 1.6, 3.2, 6.4, 12.8$) and with $h_0/H_\infty = 0.5$. These simulations covered a range of subcritical upstream Froude numbers (i.e., $F_\infty = 0.2$–0.9), and with some interpolation, accurate critical peak, and gap height values (M_p and M_g) could be determined. A subset of gap Froude number profiles for the $G = 6.4$ case is shown in Fig. 2. In all the idealized runs, the hill heights, h_0, were kept constant so that a fixed relationship existed between gap width (G) and gap height (M_2) given by (10).

The regime diagram shown in Fig. 3 summarizes the results of these calculations. On this diagram, the ordinate is both the height of the peaks and the gap. As h_0 in Fig. 3 is fixed (i.e., $h_0/H_\infty = 0.5$), the gap height is a proxy for gap width. The wider the gap, the lower the gap height. Three reference curves are shown in Fig. 3; the critical heights from (5) with $D_c = 0.5$, 1.0, and 2.0. These curves illustrate the role of horizontal confluence and difluence.

Our initial step was to estimate the conditions that cause critical conditions over the hill peaks. As these numerical results differed little from the results for a single isolated peak found previously by SS93, we have just replotted their values (curve M_p in Fig. 3). The influence of the other nearby peak seems to be small in this regard, at least for $G \geq 1.6$. The position of curve M_p in relation to the curve for a ridge C_1 suggests that there is significant difluence over an isolated hill, increasing the terrain height needed to generate critical flow. As the empirical curve (M_p) passes through the point $F_\infty = 1$ and $M = 0$, we can surmise that the difluence factor D_c approaches unity there. And, as the curve approaches the point $F_\infty = 0$ and $M = 1$ with a

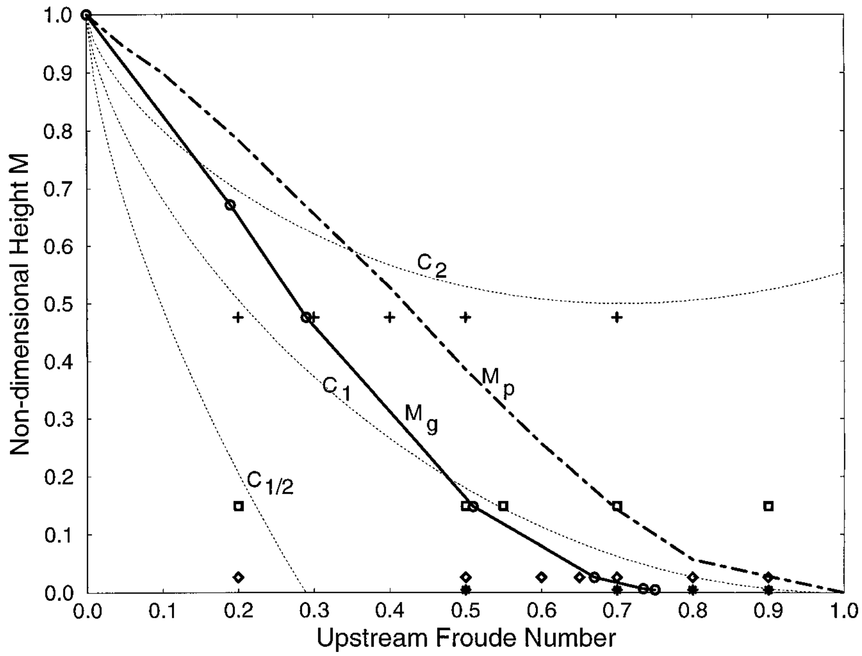

FIG. 3. A M–F_∞ regime diagram for a two-hill terrain with a fixed value of h_0/H_∞ (=0.5) and variable gap width (G). The quantity M is the nondimensional peak or saddle height. Three dotted reference curves are shown; curves C_1, C_2, and $C_{1/2}$ are based on Arakawa's formula (5) with channel width ratio $D_c = 1$, 2 (i.e., difluence) and 0.5 (i.e., confluence). Reference curve M_p is the critical value of M_1 for a single peak from (SS93a). Curve M_g is the critical value of M_2, computed for gap flow using the SWM. Symbols (cross, square, diamond, asterisk) represent runs with different gap width (G = 1.6, 3.2, 6.4, 12.8). Note that for a certain height M, curve M_p is located to the right of C_1, indicating that, due to difluence, a larger ambient Froude number is required to produce critical conditions over a peak than a ridge. Curve M_g crosses C_1, indicating that for a high narrow gap, difluence delays the onset of criticality, whereas for a low wide gap, confluence promotes criticality at the saddle.

finite slope [unlike Eq. (4)], the difluence D_c must approach infinity there. This large difluence is connected with the existence of a stagnation point at the mountain top under this limiting condition. The behavior of the critical difluence factor (D_c) near both limits ($F_\infty = 0$, 1) is qualitatively similar to the simple function $D_c = F_\infty^{-1/2}$ insofar as (5) is concerned.

From Fig. 3, it is evident that the critical curve for gap flow M_g is considerably different than either the critical curve C_1 for a ridge or curve M_p for an isolated hill. Curve M_g shows that for wide gaps (i.e., $G > 3$), the critical nondimensional gap height is less than C_1, the critical height for flow over a long ridge. This difference is due to horizontal confluence, which adds to the effect of rising terrain as the flow approaches the gap. For the largest gap width considered, $G = 12.8$, the empirical curve $M_g(F_\infty)$ in Fig. 3 goes nearly to zero for a Froude number of about $F_\infty = 0.75$. Using (5) to solve for the confluence factor, we obtain $D_c = 0.81$. Thus a 19% confluence is sufficient to bring $F_\infty = 0.75$ flow to a critical state with little if any rising terrain.

For higher narrower gaps (i.e., $G < 3$) the critical gap curve lies above the curve for an infinite ridge C_1. This result is caused by flow difluence. As the flow approaches from upstream, it has a tendency to diverge around the double-peaked obstacle. Only when it is close to the hilltop does it sense the narrow gap. Any confluence near the entrance to the gap is overwhelmed by the difluence upstream.

The reader will note that we have limited our regime diagram to subcritical upstream flow (i.e., $F_\infty < 1$). There are three reasons for this. First, several supercritical runs were carried out, without finding evidence of the long isolated gap winds we were seeking. Second, the existence of supercritical conditions (i.e., fast flow and/or weak stratification) tends to promote vertically propagating nonbreaking mountain waves, as described by linear theory. As shown in section 1b(1), this type of dynamics does not produce gap winds. Finally, the four real cases described in section 5 had subcritical upstream conditions.

d. The occurrence of gap winds

In this section, we illustrate the structure of jets and wakes for each of the three classes A, B, and C, with subcritical upstream conditions. In our three illustrations, we keep $h_0/H_\infty = 0.5$ and the nondimensional gap

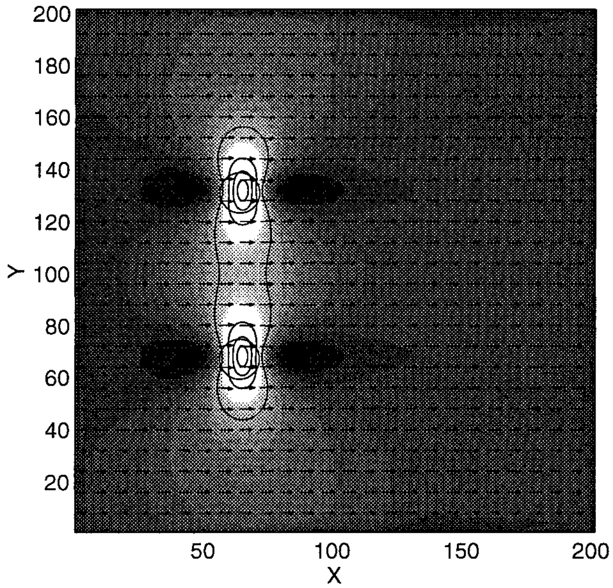

Fig. 4. A simulated flow field over two peaks in regime A (i.e., $M_1 < M_p$ and $M_2 < M_g$). The flow speed is shown in shades of gray with light/dark shades indicating fast/slow flow, similar in format to a SAR image. The wind vectors are also plotted in this figure. The upstream Froude number is 0.2. The nondimensional gap width and peak height are 6.4 and 0.5, respectively.

width is $G = 6.4$. Using (9) and (10), the nondimensional peak and gap heights are $M_1 = 0.5$ and $M_2 = 0.0265$, respectively. We change the Froude number from 0.2 to 0.6 to 0.8 to change classes from A to B to C.

1) Class A: $M_1 < M_p$ and $M_2 < M_g$

When all of the nondimensional mountain heights are less than their corresponding critical values, the flow will remain subcritical everywhere in the domain. Some potential energy is converted temporarily to kinetic energy and the flow reaches its maximum velocity along ridge line. As the flow reaches the lee slopes, the kinetic energy is converted back to the potential energy and the flow velocity returns to the speed of the upstream flow. No jet occurs in the lee of the gap (Fig. 4).

2) Class B: $M_1 > M_p$ and $M_2 < M_g$

In this case, the flow over the mountain peaks will transition from subcritical to supercritical and continue to accelerate over the lee slopes until a hydraulic jump occurs. When hydraulic jumps appear, a wake is formed downstream from each peak. Along the gap axis, since $M_2 < M_g$, the flow always remains subcritical. The speed of the flow in the gap reaches its maximum value at the saddle point of the gap, then it returns to the speed of upstream flow. The gap flow does not experience any significant reduction of the Bernoulli function because no hydraulic jump exists in the lee of the gap. Therefore,

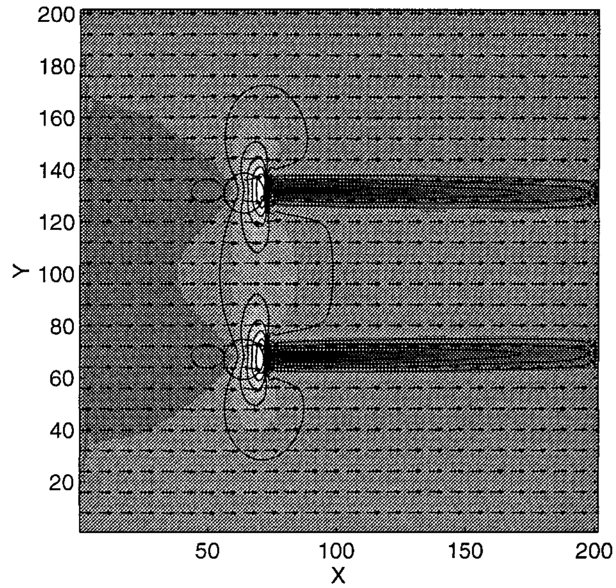

Fig. 5. Similar to Fig. 4 but for regime B ($F_\infty = 0.6$).

in the lee of the complex terrain, the speed of the flow downstream of the gap is larger than that of the adjacent wake flows (Fig. 5). We call this a subcritical gap jet. (In section 6 we explain how subcritical jets can exceed the upstream flow speed.)

3) Class C: $M_1 > M_p$ and $M_2 > M_g$

If $M_1 > M_p$ and $M_2 > M_g$, the incoming flow will transition to supercritical all along the ridge line, including the gap, and continue to accelerate in all of the lee regions until a hydraulic jump occurs. Figure 6

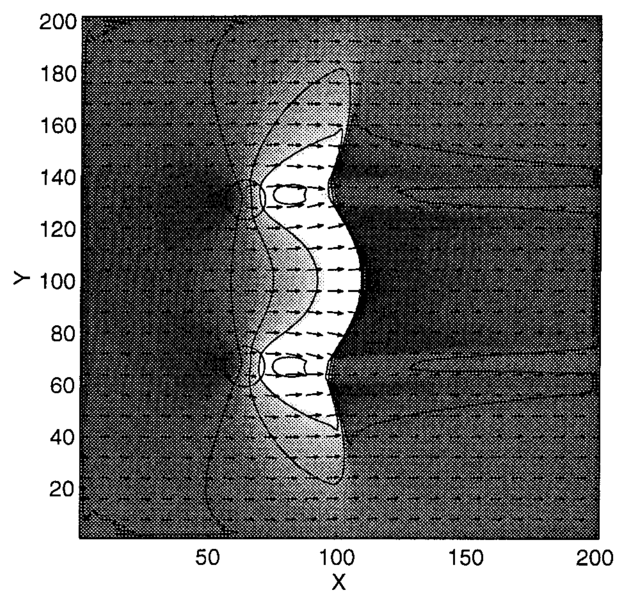

Fig. 6. Similar to Fig. 4 but for regime C ($F_\infty = 0.8$).

shows that a broad supercritical region appears in the lee of the gap. This region is slightly longer than the supercritical regions behind the peaks, but it does not have the appearence of a narrow jet.

In these three illustrations, we have chosen $M_1 \approx h_0/H_\infty = 0.5$. Other values give somewhat different patterns. A larger $M_1 = 0.8$, for example, modifies the flow shown in Fig. 6 to have much stronger wakes behind the peaks, and the wakes begin closer to the peaks.

3. Unimak Island

Unimak Island is located in the Aleutian Chain, southwest of the Alaskan Peninsula, near (54°50′N, 136°50′W). It contains five volcanic peaks above 1500 m: Shishaldin volcano (2857 m), Isanotski Peak (2494 m), Roundtop Mountain (1908 m), Pogromni volcano (2002 m), and Faris Peak (1686 m) (Fig. 7). As Faris Peak and Pogromni are very close to each other, we consider them as a single mountain (i.e., Mt. FP). Also, we call Shishaldin, Isanotski Peak, and Roundtop Mountain, Mts. S, I, and R, respectively. From the topography profile of Unimak Island (Fig. 7b), we note that there are two kinds of mountain gaps in Unimak Island; the narrow (15 km) and high (about 800 m) gap between Shishaldin and Isanotski Peak (gap S–I) and the wide (40 km) and low (about 400 m) gap between Mt. FP and Mt. S, (gap FP–S). These two different gaps provide good conditions to study the influence of gap geometry on gap winds. Another favorable aspect of Unimak Island as a dynamical laboratory is that there is a rawinsonde station—Cold Bay station (55.2°N, 162.72°W) 50 km to the northeast of this island. This observation point, however, is disturbed by Frosty Peak during southerly flow. Another station, St. Paul at 57.15°N, 170.21°W in the Pribilof Islands, 500 km northwest of Unimak Island, provides additional information about upstream flow when the wind blows from the north.

Due to its high latitude ‘‘belt of storms’’ location, the regional wind field around Unimak Island is complex and unsteady. Generally, during the winter season, the dominant synoptic features are the low in the Gulf of Alaska and high pressure center over the Bering Sea. The geostrophic wind is often northeasterly when high pressure over the Bering Sea dominates, or northerly when the low pressure center over the northern Gulf of Alaska dominates (Overland and Hiester 1980; Bond and Macklin 1993). During the summer season, as Pacific cyclones approach Unimak Island, the ambient wind is southerly or southwesterly. Atmospheric vortex shedding induced by Unimak island is well known (e.g., Chopra 1973; Thomson et al. 1977; Etling 1989). These shedding vortices can be detected by cloud patterns in visible and infrared satellite imagery. However, atmospheric vortex shedding is not the only mesoscale meteorological phenomenon induced by Unimak Island. Mountain wakes, katabatic winds, trapped lee waves, and other dynamical processes also exist in this region. Because Unimak Island is usually cloud covered, neither infrared nor visible imagery gives reliable information about sea surface wind fields near the island. SAR imagery provides a valuable new tool for such studies (Pan 1997).

4. *ERS-1* SAR imagery

The *ERS-1* satellite, one of the European Space Agency's European remote sensing satellites, operates in sun-synchronous orbit, passing overhead two times each day, one in ascending mode, the other in descending mode. The SAR aboard the *ERS-1* operates at a frequency of 5.3 GHz (C-band) with vertical polarization and an incidence angle of 23° at the midswath. The image mode of SAR obtains strips of high-resolution imagery 100 km in width to the right of the satellite track. The 10-m long antenna, aligned parallel to the flight track, directs a narrow radar beam onto the earth's surface over the swath. High-resolution images of backscatter amplitude are constructed from the time delay, frequency, and strength of the Doppler-shifted return signals. Clouds are nearly transparent to C-band microwave radiation.

The radar backscatter responds to surface roughness and hence to phenomena that affect ocean wave spectra. Predominate among these phenomena is the sea surface wind. Mesoscale meteorological phenomena generate wind variations in the atmosphere boundary layer changing the sea surface roughness, which in turn is sensed by SAR as changes in the local radar backscatter coefficient. Since *ERS-1* was launched in July 1991, its SAR images have been widely used to study mesoscale meteorological phenomena, for example, atmospheric gravity waves (Thomson et al. 1992; Vachon et al. 1995), lee waves (Vachon et al. 1994), convection (Sikora et al. 1995), and convective storms (Atlas and Black 1994).

In this project, we used low resolution (100 m) *ERS-1* SAR images preprocessed at the Alaska SAR Facility (ASF). Each image covers about 100 km × 100 km area and contains 1024 × 1024 pixels. To keep each SAR image the same size, ASF regrouped each whole track dataset into several 1024 × 1024 × 1 byte images. We mosaiced two or three images to generate one image covering a larger area.

To generate a wind speed field from the digital number values (DN) in the SAR image, a number of steps were taken. First, the dimensionless normalized backscatter coefficient is computed from

$$\sigma_0 = 10 \log_{10}(a_2 DN^2), \tag{11}$$

where a_2 is the gain factor provided by the ASF. The strong dependence of backscatter on incidence angle is removed by defining the effective backscatter coefficient $\sigma_{\rm eff}$ at the center of the range ($x' = 512$):

$$\sigma_{\rm eff} = \sigma_0 + 0.0044(x' - 512), \tag{12}$$

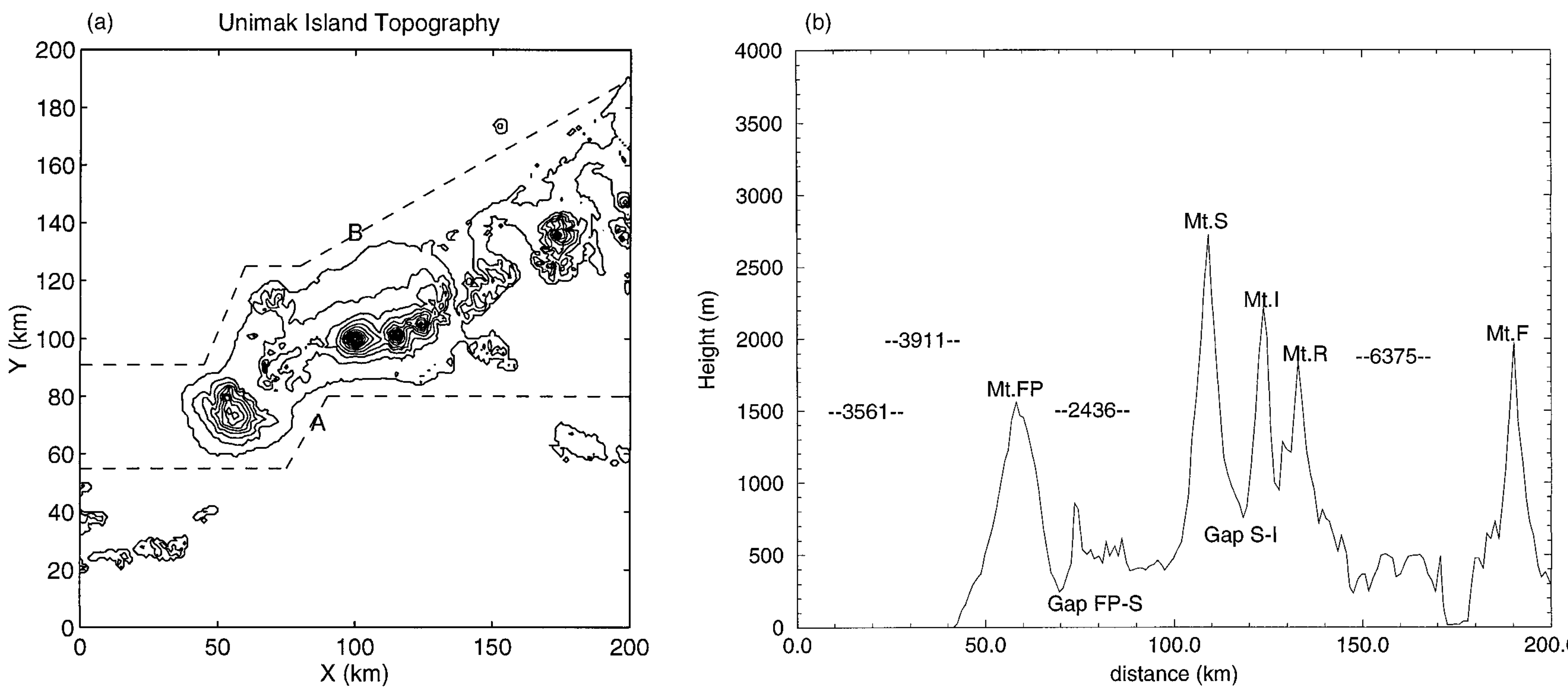

FIG. 7. (a) Topographic contours of Unimak Island. The contour interval is 200 m. Transects A and B are used for wake–jet analysis. (b) The island profile as seen from the south-southeast. The mountains marked FP, S, I, R, F are Faris/Pogromni, Shishaldin, Isanotski, Roundtop, and Frosty. The vertical exaggeration is 40 to 1. Free surface heights for the four simulations are shown dashed.

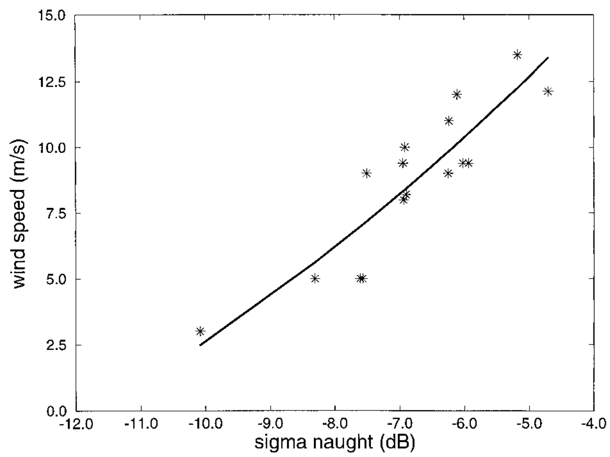

FIG. 8. *ERS-1* wind speed calibration curve using SAR and balloon data near St. Paul station in the Pribilof Islands. The fitted curve is given by (13).

where x' is the pixel number in the direction perpendicular to the satellite path. The slope 0.0044 is determined by averaging transects on several images with large undisturbed areas. Finally, the wind speed is computed from $\sigma_{\rm eff}$ by neglecting the influence of wind direction and using the empirical formula

$$|U| = a + b\sigma_{\rm eff} + c\sigma_{\rm eff}^2, \qquad (13)$$

where $a = 26.41$, $b = 3.11$, and $c = 0.0733$, and U are expressed in meters per second.

The coefficients in (13) were determined from 16 calibration points derived from open-ocean *ERS-1* SAR imagery and balloon soundings from St. Paul station in the Pribilof Islands (Fig. 8). This self-calibration procedure was felt to be more accurate and self-consistent than using existing wave-scattering models (e.g., Malinas et al. 1992; Shuchman et al. 1993). The final fields of $|U/U_\infty|$ (Fig. 9) are computed by dividing $|U|$ from (13) with an average value from (13) for the upstream region.

5. Comparison of SAR and SWM flow fields

a. Procedures

As discussed in section 4, processed *ERS-1* SAR images provide information about the sea surface wind speed patterns relative to upstream values. To carry out a comparison between SAR and the SWM, we downloaded about 100 SAR images from the Alaska SAR facility and selected a few for detailed analysis. Because the ridge line of Unimak Island runs east–west and *ERS-1* SAR imagery gives wind field information only over ocean, we chose to examine SAR images when the background wind is primarily meridional. Meridional flow passing over the mountains will quickly reach the ocean surface and can be detected by *ERS-1* SAR imagery. If the wind blows zonally, wakes interfere with each other, jets are absent or ill-defined and exist over the land surface where they can not be detected by SAR imagery. Also we selected *ERS-1* SAR images, which had interesting gap wind patterns and evidence of layered atmospheric structure in balloon soundings. Of approximately 40 available SAR images with meridional flow, we have chosen four with marked inversions or reverse shear, consistent wind directions and well-defined wake features (Fig. 9). For the selected cases, we used soundings from Cold Bay, close to the acquisition time of the SAR images, to estimate the free parameters of the upstream flow for the numerical experiments. We also consulted the National Centers for Environmental Prediction–National Center for Atmospheric Research (NCEP–NCAR) (Kalnay et al. 1996) 1000-mb geopotential height contours for upstream wind speed and wind direction.

For each of the four selected cases, the single layer shallow water model was run using upstream flow from the available soundings (Fig. 10). Generally, the height of the inversion layer was chosen as the free surface height H_∞, the reduced gravity g' was determined from the increment in potential temperature across the inversion layer (e.g., $\Delta\theta = 5$ K, $\theta = 280$ K, $g' = \Delta\theta{*}g/\theta = 0.18$), and θ is the average potential temperature of this layer. The undisturbed upstream wind speed, U_∞, was taken from the sounding as the average value below H_∞.

All the runs were done without considering bottom friction and earth rotation. Because the length scale in cross island direction is about 40 km and the undisturbed upstream wind speed is about 10–20 m s^{-1} for our cases, the Rossby number is $R = U/fL = 2.5$, suggesting that the Coriolis force will only play a minor role. As argued in Smith et al. (1997), the length scale for wake decay by bottom friction is about 300 km over the sea, so for near wake studies, friction can be neglected.

The gridded domain covers 200 × 200 km with a grid interval of 1 km. The peak of Shishaldin volcano was chosen as the center of this domain [i.e., the point (100, 100)]. The identification number for each case is the identification number of the *ERS-1* SAR image. We suspect, and numerical simulations indicate, that the four cases we considered were unsteady due to a changing environment and wake instability. Rather than attempt to choose the moment from the simulation that best matches the SAR ''snapshot,'' we have run each simulation to a standard time of 2000 units. Hence our comparison of wake–jet geometry can only be quali-

→

FIG. 9. Four processed *ERS-1* SAR images. Shade of gray indicates the ratio of flow speed to upstream value using (13). Table 2 describes the image conditions. The interesting coastal wind features are marked by letters: **a, b, c, d,** . . . .

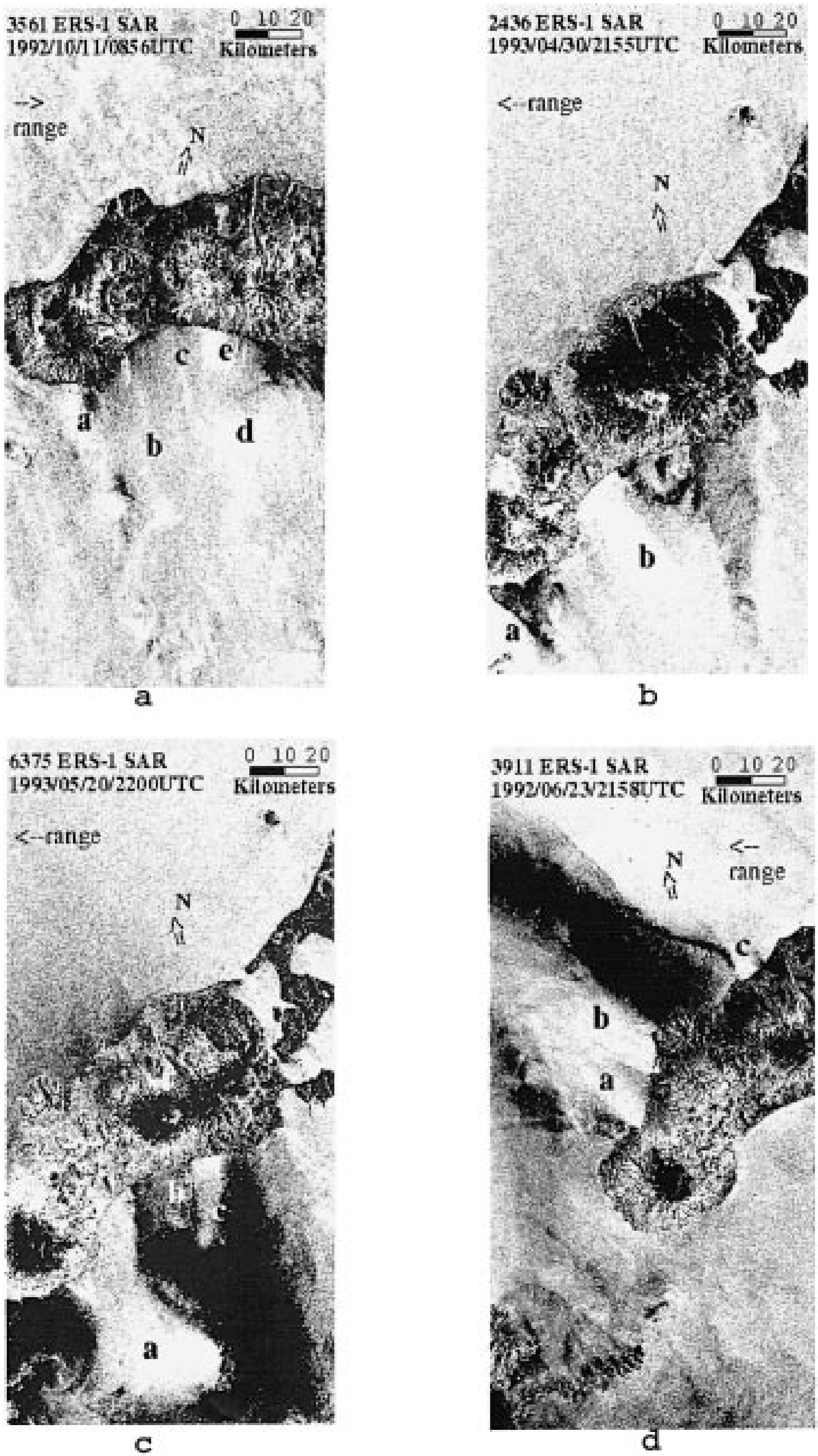
3561 ERS-1 SAR
1992/10/11/0856UTC
0 10 20
Kilometers
--> range
N
a
2436 ERS-1 SAR
1993/04/30/2155UTC
0 10 20
Kilometers
<--range
N
b
6375 ERS-1 SAR
1993/05/20/2200UTC
0 10 20
Kilometers
<--range
N
c
3911 ERS-1 SAR
1992/06/23/2158UTC
0 10 20
Kilometers
<--
range
N
d

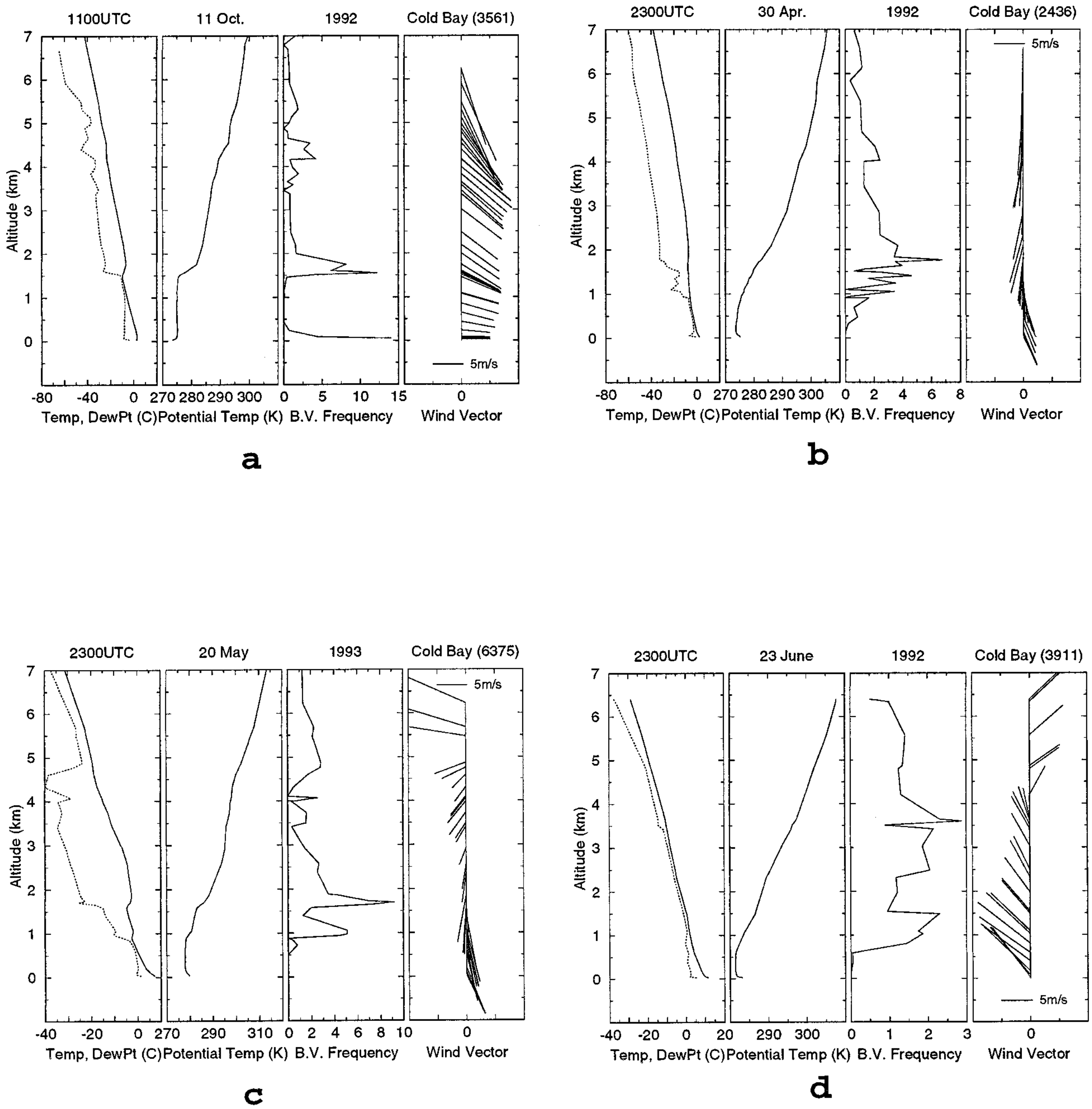

FIG. 10. Sounding data obtained at Cold Bay station, corresponding to the four SAR images in Fig. 9. Figure includes temperature, dewpoint temperature (dotted), potential temperature, the Brunt–Väisälä frequency and wind vector profiles. Table 2 lists the parameters deduced from these soundings.

tative. Nevertheless, we attempt to identify particular SAR-observed flow features (i.e, labeled **a, b, c,** . . .) that agree or disagree with the SWM simulations. Basic data for the four cases are given in Table 2. Layer depths are also shown in Fig. 7b.

Two graphical methods of comparison are used. First, the horizontal pattern of wind speed from the SWM is presented in grayscale (Fig. 11), a similar format to the SAR image (Fig. 9). To supplement the grayscale wind speed pattern, a zoomed map of local Froude number is given to aid in diagnosis (Fig. 12). Second, wind speeds from the model and the SAR image are taken along a segmented transect close to the lee coast of Unimak (see Fig. 7) and plotted against zonal distance (Fig. 13).

b. Results

All four cases had roughly similar values for the control parameters (Table 2). The layer depth was about

TABLE 2. Parameters for numerical simulations and SAR imagery of Unimak airflow.

Case	3561	2436	6375	3911
H (m)	1500	1500	1880	2000
θ (K)	280	277	282	286
$\Delta\theta$ (K)	7	7	8	8
Upstream wind speed (m s^{-1})	10	8	10	11
Upstream wind direction (deg)	315	340	345	140
F_∞	0.52	0.42	0.44	0.47
U_∞	0.37	0.14	0.114	−0.30
V_∞	−0.37	−0.39	−0.425	0.36
Dimensionless time units	2000	2000	2000	2000
Date & time of SAR image	11 Oct 92 0856 UTC	30 Apr 92 2155 UTC	20 May 93 2200 UTC	23 Jun 92 2158 UTC
Date & time of sounding data	11 Oct 92 1100 UTC	30 Apr 92 2300 UTC	20 May 93 2300 UTC	23 Jun 92 2300 UTC

1700 m giving nondimensional mountain heights of about $M_1 = 0.9$ and 1.3 for Mts. FP and S. The nondimensional gap heights were about $M_2 = 0.2$ and 0.5 for gaps FP–S and S–I. The upstream Froude numbers were about 0.47, which, from Fig. 3, gives $M_p = 0.5$ and $M_g = 0.25$. As $M_1 > M_p$, we expect that all the peaks should generate supercritical flow and wakes. The low gap FP–S has $M_2 < M_g$ and therefore should retain subcritical flow. The high gap S–I has $M_2 > M_g$ and so it should generate weak supercritical flow.

Several common features can be seen in all four of the SWM and SAR results (Figs. 9, 11, 12, 13). Each SWM run gave (from west to east), a Mt. FP wake, a jet from gap FP–S, a wake from Mt. S–I–R, with an embedded jet from gap S–I. The SAR images are more variable, but each shows a relatively uniform upstream environment and disturbed downstream patterns. Three of the cases show only two or three of the four predicted jet–wake features. Only case 6375 clearly shows all four predicted features. Also, the general shape of the wake region is much simpler in the SWM results than in the SAR images, although both fields are complex. A brief description of each case is given below.

1) CASE 3561

This is a case with NW winds giving a wake–jet pattern to the south of Unimak. In the SAR image, periodic shedding eddies are seen from Mts. FP and S. Both eddy trains have a wavelength of about 40 km. The jet FP–S is weak or missing but the jet from gap S–I is present. A wake from Mts. S–I is evident.

The upstream temperature profile (Fig. 11a) showed that there was an inversion layer from 1500 m to 1800 m. No strong wind shear existed. For the SWM, we chose 1500 m as the free surface height H_∞. The upstream Froude number is 0.52. All the peaks generate strong supercritical flow and wakes. The model captures the eddy train from FP with a wavelength of 50 km. The jet through FP–S reaches $F = 0.7$ whereas the jet through S–I becomes briefly supercritical with $F = 1.8$ before forming a long narrow subcritical jet with $F \approx 0.8$ (Fig. 12a). Both predicted subcritical jets extend downstream over the water where they could be detected by SAR.

2) CASE 2436

This case had winds from the north-northwest giving wake–jet patterns to the south of Unimak. The SAR image showed a corner wind SW from Mt. FP, a wake from FP, a jet from gap FP–S, and a wake from Mt. S–I–R with an imbedded jet from gap S–I.

From the Cold Bay sounding data (see Fig. 11b), there was no strong inversion layer but a reversed wind shear was present at about 1500 m. Therefore, we chose 1500 m as the free surface height. The SWM Froude number structure (Fig. 12b) was similar to the previous case (Fig. 12a). All the peaks generate strong supercritical flow and wakes. Gap wind FP–S was subcritical and S–I went briefly supercritical.

3) CASE 6375

This case also had winds from the north-northwest giving wake–jet patterns to the south of Unimak. The SAR image shows a wake from FP, a jet from gap FP–S, a wake S–I–R, with an imbedded jet from gap S–I. Slight upstream blocking is present.

From the Cold Bay sounding data (Fig. 11c), we can see that there existed two inversion layers, one located at about 1000 m, the other was at 1880 m. We chose 1880 m as the free surface height H_∞ as it was coincident with reverse wind shear. The model captured both major wakes and jets. The jet FP–S reached $F = 0.6$ in the gap while jet S–I went briefly supercritical in the gap and was shocked to a subcritical condition with $F = 0.8$ (Fig. 12c).

4) CASE 3911

This case had winds from the southeast giving a wake–jet pattern to the north of Unimak. The SAR image shows a wake from FP, a jet from gap FP–S, and

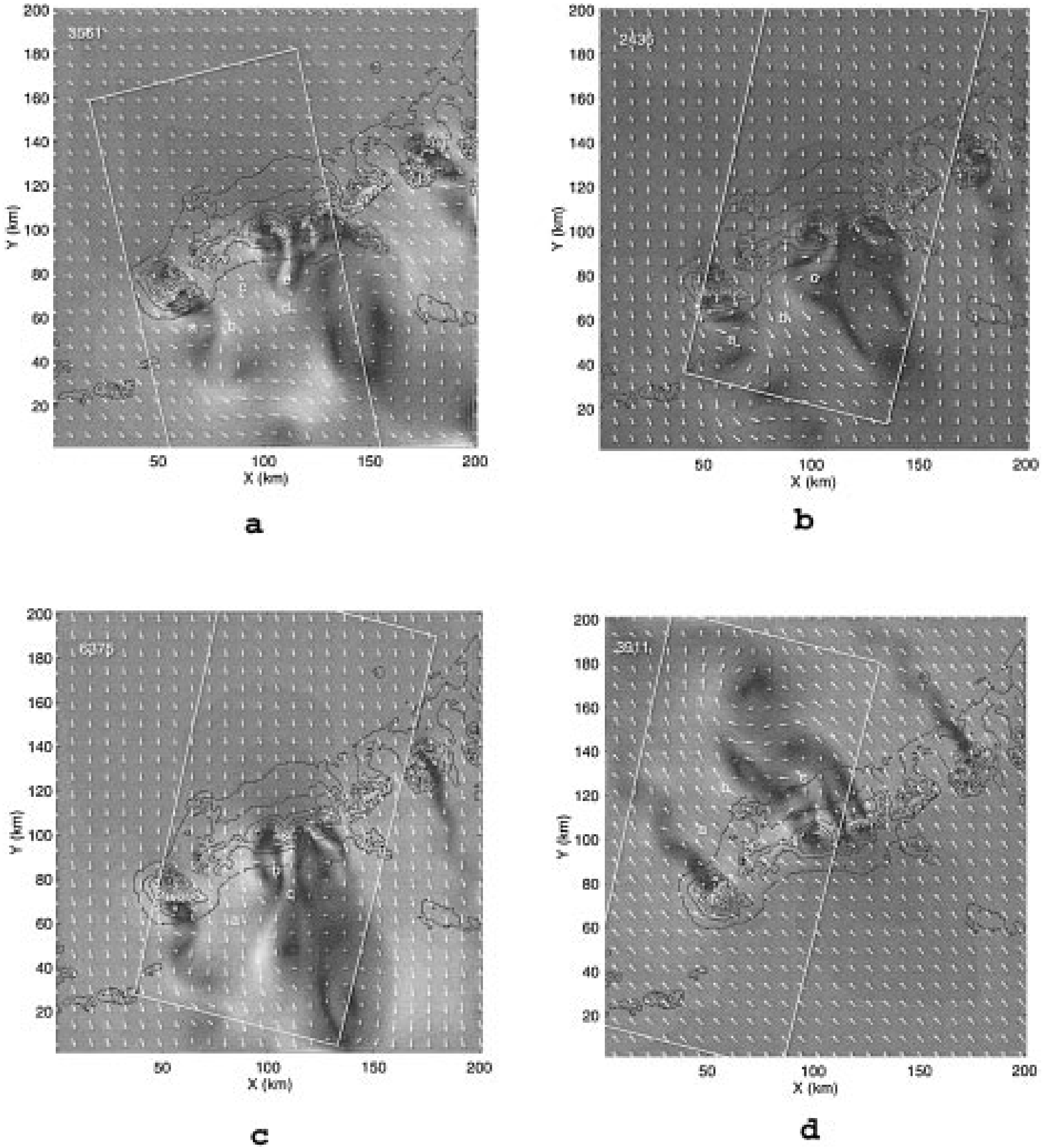

FIG. 11. Simulated flow fields using the SWM corresponding to the four SAR images in Fig. 9. Shade of gray indicates the nondimensional flow speed. Wind vectors are also shown. Letters **a, b, c, d** correspond to the same features marked in SAR image. Rectangles show the location of the SAR data in Fig. 9.

a wake from S–I–R. A broad triangular region of moderated speed nearly filling wake S–I–R could be interpreted as an imbedded jet from gap S–I.

From the Cold Bay sounding, there was no sharp inversion layer, but reverse shear existed above 1500 m. We chose 2000 m as the free surface height. The wakes from FP and S–I–R, and the jet FP–S, are captured. The flow in gap FP–S stayed subcritical with $F = 0.6$, whereas the flow in gap S–I went marginally critical and returned to $F = 0.5$ (Fig. 12d).

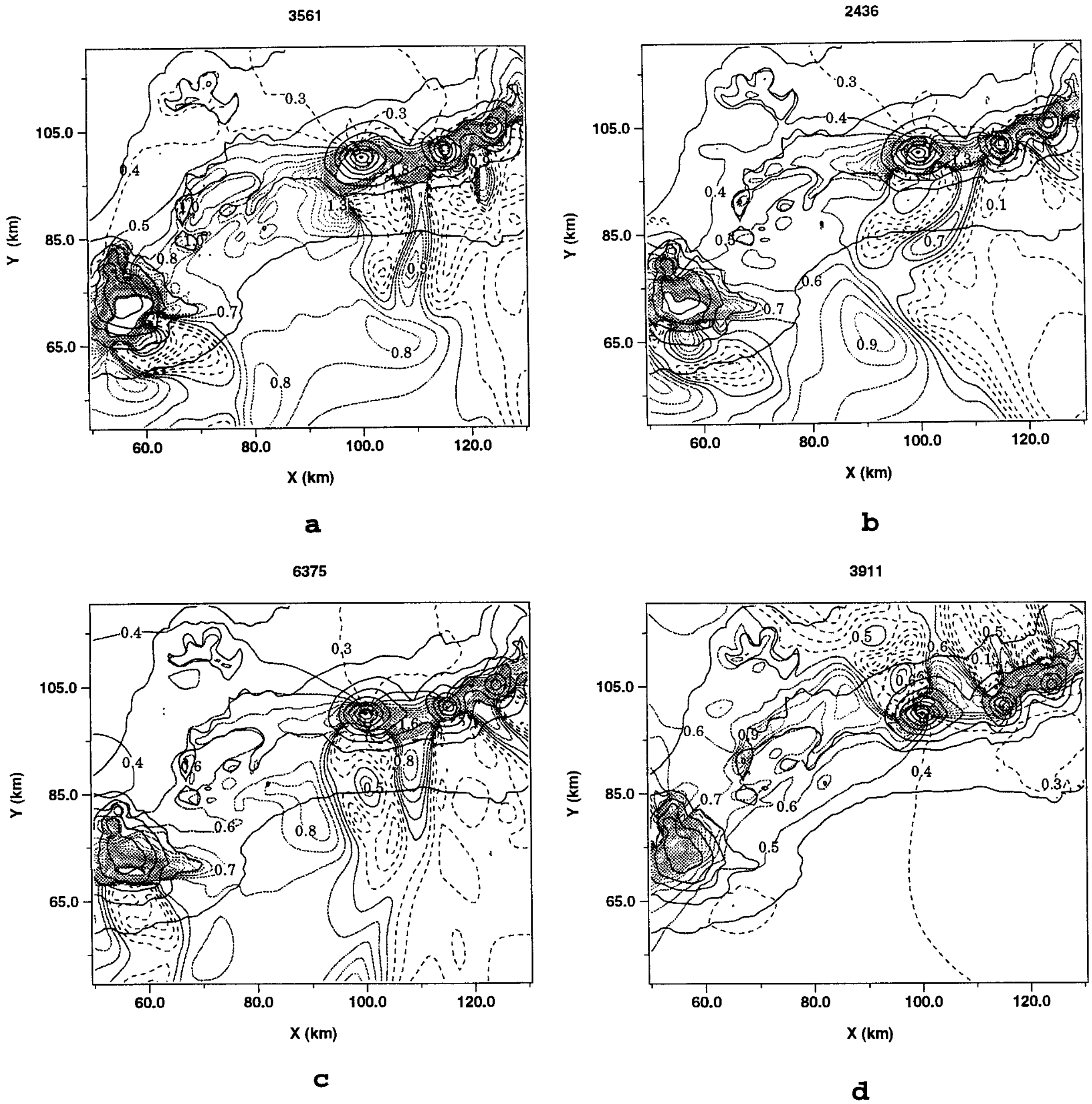

FIG. 12. Zoom maps of local Froude numbers from the four simulations shown in Fig. 11. The contour interval is 0.1. Dense dotted lines are $F > F_\infty$. Dashed contours indicate $F < F_\infty$. Terrain contours are solid lines. Holes indicate that hills have pierced the free surface. This diagram is used to judge the sub- or supercritical nature of the flow through gaps FP–S and S–I. Mt. Shishaldin is located at coordinates (100, 100).

c. Summary of comparisons

Overall, the agreement between the SWM and SAR wind speed patterns is only fair. The simulated wakes and jets are in about the right place and exhibit the proper speeds relative to the upstream speed.

There are several possible reasons for the lack of quantitative agreement. First, the upstream conditions are poorly known. Neither the Cold Bay sounding nor the NCEP–NCAR reanalysis give accurate representative upstream conditions. An error in upstream wind direction causes the predicted wakes and jets to be shifted with respect to their actual locations. Furthermore, the choice of shallow water parameters g', H_∞, and U_∞ is rather imprecise. Second, we have ignored unsteadiness in the upstream conditions and fluctuations caused by wake instability. We have simply compared inde-

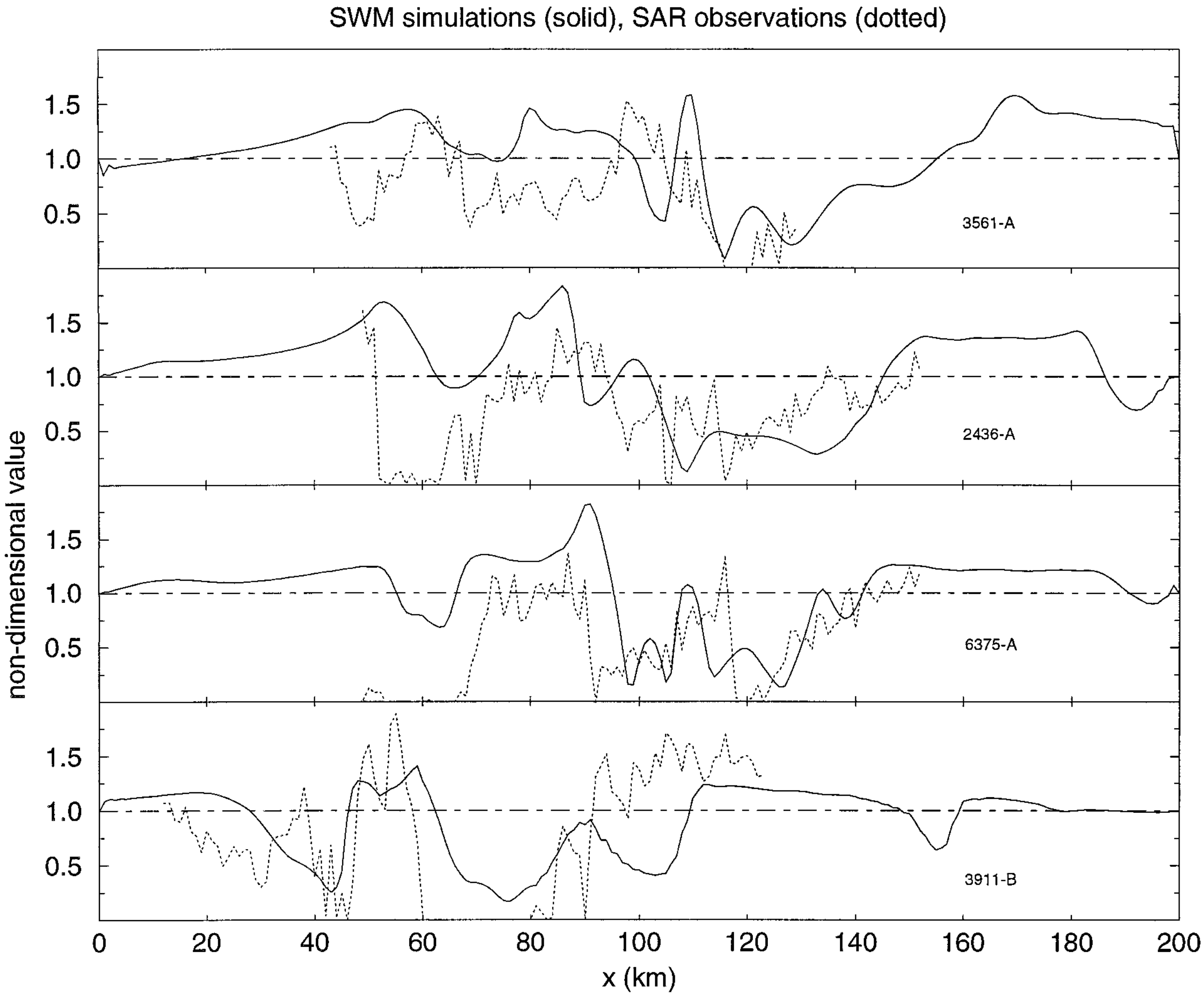

FIG. 13. Wind speed ratio (U/U_∞) along leeside transect (A or B, see Fig. 7a), from SWM (Fig. 11) and the SAR images (Fig. 9).

pendent ‘‘snapshots’’ from nature and the SWM. Finally, the SWM is highly idealized.

6. Bernoulli function control of jets and wakes

A deeper understanding of jet–wake phenomena can be found by considering the streamline by streamline relationship between Bernoulli function and wind speed. With uniform upstream conditions, Bernoulli function variations in the wake are determined by the strength of the jump over the terrain that each streamline passed through.

The dimensional Bernoulli function for shallow water flow is

$$\hat{B} = \frac{1}{2}\rho\hat{U}^2 + \rho g(\hat{H} + \hat{h}). \tag{14}$$

A simpler nondimensional form of (14) for diagnosing SWM wakes is

$$B = \frac{\hat{B}}{\rho g \hat{H}_\infty} = \frac{1}{2}U^2 + H, \tag{15}$$

where $U^2 = \hat{U}^2/g'\hat{H}_\infty$, $H = \hat{H}/\hat{H}_\infty$, and $\hat{h} = 0$. Transposing (15)

$$U^2 = 2[B - H] \tag{16}$$

indicates that the Bernoulli function (B) and pressure (H) control the fluid speed in steady regions where $h(x, y) = 0$.

The relationship between U^2 and B is plotted in Fig. 14a for the wake simulation shown in Fig. 5. All points fall onto (16) with $H = 1$. This indicates that the wake pressure has fully equilibrated with the ambient pressure. The only factor controlling wind speed is the Bernoulli loss suffered by each streamline as it passed over the terrain.

Figure 14b shows the relationship between U^2 and B along a transect about 60-km downwind of Unimak Island for the simulation of case 6375 (Fig. 11c). Most

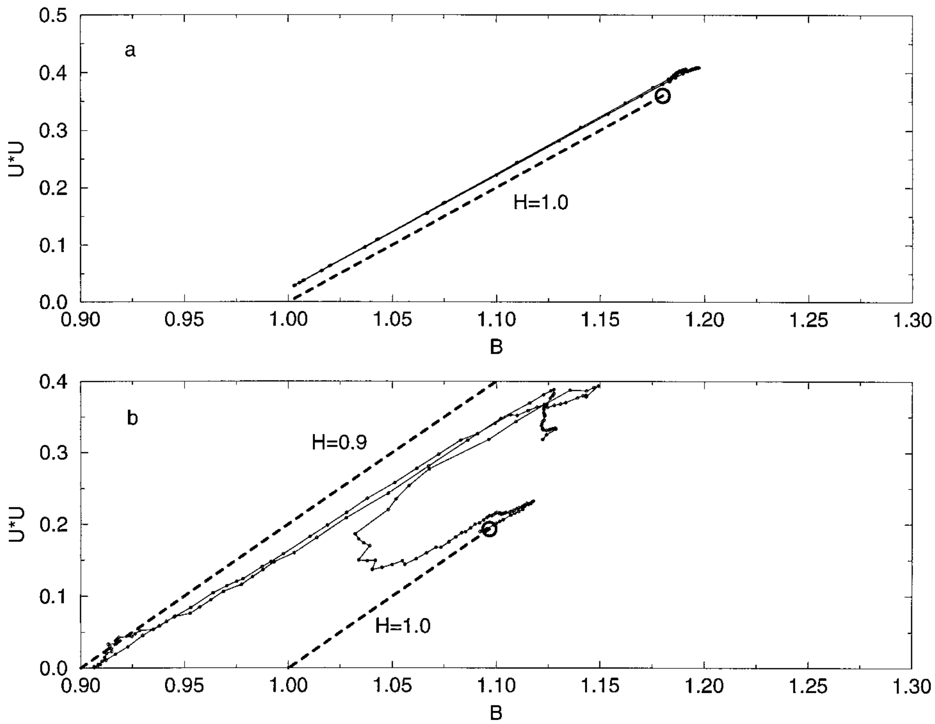

FIG. 14. The relationship between Bernoulli function and flowspeed downstream of terrain: (a) for a two-hill flow (Fig. 5, along $x = 100$) and (b) for realistic Unimak terrain [case 6375, Fig. 11c, along $y = \tan(15°)x$]. Jets and wakes lie along "pressure equilibrated" lines given by (16) with H = constant. The heavy circle indicates the specified upstream condition.

of these data fall on a line given by (16) with $H = 0.9$ indicating that the local jet and wake patterns have equilibrated to a common regional pressure, but this (scaled) pressure is 10% less than the ambient upstream value. This lower pressure allows the airstreams with undepleted Bernoulli function to attain speeds considerably greater than ambient. Wind speeds reaching twice the ambient value are seen. Only in the lower left of Fig. 11c do the U^2 and B values fall on the $H = 1$ reference curve.

The primary difference between Figs. 14a and 14b is the terrain shape. The two-hill terrain is relatively isolated while Unimak Island forms a ridgelike barrier with length $L \sim 100$ km. As the air deflected around this ridge curves inward, centripetal forces allow the regional wake pressure to maintain a value lower than the ambient pressure. We refer to the part of the downstream region with reduced pressure as the "near wake." Its downwind extent is the order of the ridge length L. Gap winds in the near wake can exceed upstream speeds. Farther downstream, the pressure fully equilibrates ($H = 1$) and gap winds cannot exceed upstream speeds. They retain their jetlike character, only with respect to the adjacent wakes with reduced Bernoulli function.

The reader may note that a few of the Bernoulli values in Figs. 14a and 14b are slightly greater than specified inflow value. This discrepancy is due to a slight misadjustment between the specified inflow boundary condition and the actual upstream flow.

7. Conclusions

The goal of this study was to develop a new conceptual model of mountain gap winds, using a shallow water model (SWM). The SWM was then partially verified with synthetic aperture radar (SAR) images of wind waves near Unimak Island.

The new conceptual model has three elements:

- the role of difluence and confluence over complex terrain in generating supercritical flow;
- the relationship between hydraulic jumps in the downslope region, and jets and wakes farther downstream;
- local and regional pressure equilibration in the wake region.

The first conceptual element is the role of horizontal airflow confluence and difluence on the generation of local supercritical flow (i.e., $F > 1$) under ambient subcritical conditions. Our results show that significant difluence or confluence occurs over the upslope region in complex terrain. The effect of difluence (confluence) near a peak ($\partial^2 h/\partial x^2 < 0$, $\partial^2 h/\partial y^2 < 0$) (saddle) ($\partial^2 h/\partial x^2 < 0$, $\partial^2 h/\partial y^2 > 0$) is to retard (promote) the occurrence of supercritical flow. Thus a peak (saddle) will have a higher (lower) critical height and a higher (lower) critical ambient Froude number than will an infinite ridge with the same height. In an extreme example of confluence, flow in a level gap (i.e., $h = 0$, $\partial^2 h/\partial y^2 > 0$) can generate supercritical flow by confluence alone; with no rising terrain. However, although the effect of confluence and difluence is significant, *it is not dominant.* In both the idealized and real terrain geometries studied in this paper, critical conditions always occur first at mountain peaks, despite the influence of difluence and confluence. Thus the effect of *rising terrain dominates* over the effect of difluence/confluence. This result has broad significance in the theory of gap flows.

The second issue is the relationship between hydraulic jumps in downslope flow, and jets and wakes farther downstream. Our results include an irony. The strong supercritical flow over the peaks leads to strong jumps and Bernoulli loss, and weak flow in the wake region. The subcritical flow (or weakly supercritical flow) in the gaps experiences little or no Bernoulli loss. These streamlines maintain strong flow in the wake region.

It is important to note that supercritical flow formed just downstream of a ridgeline, peak, or gap can usually be maintained only a very short distance downstream. The maintenance and farther downslope acceleration of supercritical flow would require a very low leeside pressure. In complex or isolated terrain the leeside pressure is usually only slightly below the ambient pressure and thus the supercritical flow extends only part way down the lee slope. For this reason it is essential to distinguish between strong flows over and just downstream of the highest terrain, and jets and wakes farther downstream.

It is ironic that the most strongly accelerated flow (i.e., over the peaks) is the weakest flow farther downstream. Thus, gap flows exist downstream of complex terrain because the flow through the gap was *not* strongly accelerated and did *not* transition to supercritical flow. In a sense, the downstream gap flow is strong because it found a slow easy route over the mountains.

The third element of the conceptual model is the pressure equilibration of the wake region airstreams. Our results indicate that streamlines in the wake region with different Bernoulli values quickly equilibrate their pressures so that speed and Bernoulli values become uniquely related. In the case of a long ridge, this equilibrated pressure can be lower than ambient, allowing gap winds to exceed ambient wind speed values. Downstream of isolated or complex terrain, the equilibrated pressure will equal the ambient pressure, and gap winds cannot exceed the ambient speed.

The final concern of this paper is to demonstrate that conclusions drawn from the SWM are relevant to the atmosphere. Previous work by Schär and Durran (1997) and Smith et al. (1997) generally support this view but we turned to SAR imagery to provide more specific evidence. Four cases of SAR images from Unimak Island showed qualitative agreement with the SWM predictions. These data also provided evidence that gap winds downstream of terrain can have speeds faster than ambient speeds.

As orographic flows are inherently 3D, the modeling and observational methods used in this study cannot be regarded as complete. The SW Model oversimplifies gravity wave breaking by treating it as hydraulic jump formation on a single layer. It can be expected to give good results only in some layer-like atmospheric cases. Likewise, SAR imagery, although it is a powerful tool for mapping horizontal patterns of low-level wind speed, does not give the full 3D wind field. Future work on gap flows may require more powerful models and remote sensing techniques.

Acknowledgments. Paul Gluhosky assisted in obtaining Cold Bay sounding data and NCEP–NCAR reanalysis data and maintaining the computer hardware and software used in this study. Christoph Schär allowed us to use his shallow water code. *ERS-1* SAR images were provided by Alaska SAR Facility. Image processing was carried out at Yale Center for Earth Observation with the assistance of Art Gleason. Useful comments were provided by W. Blumen and two anonymous referees. This research was supported by the NASA/ADRO program (NAG 5-3972) administered by Dr. R. H. Thomas and by the National Science Foundation (ATM-9303825).

REFERENCES

Arakawa, S., 1969: Climatological and dynamical studies on the local strong winds, mainly in Hokkaido, Japan. *Geophys. Mag.,* **34,** 349–425.

Atlas, D., and P. G. Black, 1994: The evolution of convective storms from their footprints on the sea as viewed by synthetic aperture radar from space. *Bull. Amer. Meteor. Soc.,* **75,** 1183–1190.

Baines, P. G., 1995: *Topographic Effects in Stratified Flows.* Cambridge University Press, 482 pp.

Blumen, W., and S. C. Dietze, 1981: An analysis of three-dimensional mountain lee waves in a stratified shear flow. *J. Atmos. Sci.,* **38,** 1949–1963.

Bond, N. A., and S. A. Macklin, 1993: Aircraft observations of offshore-directed flow near Wide Bay, Alaska. *Mon. Wea. Rev.,* **121,** 150–161.

Chopra, K. P., 1973: Atmospheric and oceanic flow problems introduced by islands. *Advances in Geophysics,* Vol. 16, Academic Press, 297–421.

Clarke, A. J., 1988: Inertial wind path and sea surface temperature patterns near the Gulf of Tehuantepec and Gulf of Papagayo. *J. Geophys. Res.,* **93,** 15 491–15 501.

Colle, B. A., and C. F. Mass, 1996: An observational and modeling study of the interaction of low-level southwesterly flow with the Olympic Mountains during COAST IOP4. *Mon. Wea. Rev.,* **124,** 2152–2175.

——, and ——, 1998: Windstorms along the western side of the Washington Cascade Mountains. Part I: A high resolution observational and modeling study of the 12 February 1995 event. *Mon. Wea. Rev.,* **126,** 28–52.

Colman, B. R., and C. F. Dierking, 1992: The Taku wind of southeast Alaska: Its identification and prediction. *Wea. Forecasting,* **7,** 49–64.

Etling, D., 1989: Atmospheric vortex streets in the wake of large islands. *Meteor. Atmos. Phys.,* **41,** 157–164.

Fett, R. W., 1993: The Kamishak gap wind as depicted in DMSP OLS and SSM/I data. *Int. J. Remote Sens.,* **14,** 403–423.

Finnigan, T. D., J. A. Vine, P. L. Jackson, S. E. Allen, G. A. Lawrence, and D. G. Steyn, 1994: Hydraulic physical modeling and observations of a severe gap wind. *Mon. Wea. Rev.,* **122,** 2677–2687.

Grubišić, V., R. B. Smith, and C. Schar, 1995: The effect of bottom friction on shallow water flow past an isolated obstacle. *J. Atmos. Sci.,* **52,** 1985–2005.

Houghton, D. D., and A. Kasahara, 1968: Nonlinear shallow fluid flow over an isolated ridge. *Commun. Pure. Appl. Math.,* **21,** 1–23.

Hurd, W. E., 1929: Northers of the Gulf of Tehuantepec. *Mon. Wea. Rev.,* **57,** 192–194.

Jackson, P. L., and D. G. Steyn, 1994a: Gap winds in a fjord. Part I: Observations and numerical simulations. *Mon. Wea. Rev.,* **122,** 2645–2665.

——, and ——, 1994b: Gap winds in a fjord. Part II: Hydraulic analog. *Mon. Wea. Rev.,* **122,** 2666–2676.

Jansa, A., 1987: Distribution of the mistral: A satellite observation. *Meteor. Atmos. Phys.,* **36,** 201–214.

Kalnay, E., and Coauthors, 1996: The NCEP/NCAR 40-Year Reanalysis Project. *Bull. Amer. Meteor. Soc.,* **77,** 437–471.

Kaufmann, P., and R. O. Weber, 1996: Classification of mesoscale wind fields in the MISTRAL field experiment. *J. Appl. Meteor.,* **35,** 1963–1979.

Klemp, J. B., and D. K. Lilly, 1975: Dynamics of wave induced downslope winds. *J. Atmos. Sci.,* **32,** 320–339.

Lackmann, G. M., and J. E. Overland, 1989: Atmospheric structure and momentum balance during a gap-wind event in Shelikof Strait, Alaska. *Mon. Wea. Rev.,* **117,** 1817–1833.

Long, R. R., 1954: Some aspects of the flow of stratified fluids. Part II: Experiments with a two fluid system. *Tellus,* **6,** 97–115.

Macklin, S. A., J. E. Overland, and J. P. Walker, 1984: Low-level gap winds in Shelikof Strait. *Proc. Third Conf. on Meteorology of Coastal Zone,* Miami, FL, Amer. Meteor. Soc., 97–102.

——, N. A. Bond, and J. P. Walker, 1990: Structure of a low-level jet over lower Cook Inlet, Alaska. *Mon. Wea. Rev.,* **118,** 2568–2578.

Malinas, N. P., R. A. Shuchman, and K. Kloster, 1993: Tromso *ERS-1* calibration. *Proc. Second Scandinavian SAR Symp.,* Bergen, Norway, Nansen Environmental and Remote Sensing Center, 118–124.

Marwitz, J. D., and P. J. Dawson, 1984: Low-level airflow in southern Wyoming during wintertime. *Mon. Wea. Rev.,* **112,** 1246–1262.

Mass, C. F., and M. D. Albright, 1985: Severe windstorm in the lee of the Cascade mountains of Washington State. *Mon. Wea. Rev.,* **113,** 1261–1281.

——, S. Businger, M. D. Albright, and Z. A. Tucker, 1995: A windstorm in the lee of a gap in a coastal mountain barrier. *Mon. Wea. Rev.,* **123,** 315–331.

Masson, V., and P. Bougeault, 1996: Numerical simulation of low-level wind created by complex orography: A Cierzo case study. *Mon. Wea. Rev.,* **124,** 701–715.

McAneny, K. J., A. Baille, and G. Sappe, 1988: Turbulence measurements during mistral winds with a 1-dimensional sonic anemometer. *Bound.-Layer Meteor.,* **42,** 153–166.

Overland, J. E., and T. R. Hiester, 1980: Development of a synoptic climatology for the northeast Gulf of Alaska. *J. Appl. Meteor.,* **19,** 1–14.

Pan, F., 1997: Gap winds near Unimak Island: Numerical simulations and SAR observations. M.S. thesis, Department of Geology and Geophysics, Yale University, 92 pp.

Pettre, P., 1982: On the problem of violent valley winds. *J. Atmos. Sci.,* **39,** 542–554.

Queney, P., 1948: The problem of airflow over mountains: A summary of theoretical studies. *Bull. Amer. Meteor. Soc.,* **29,** 16–26.

Ramachandran, G., K. V. Rao, and K. Krishna, 1980: An observational study of the boundary-layer winds in the exit region of a mountain gap. *J. Appl. Meteor.,* **19,** 881–888.

Reed, R. J., 1981: A case study of a Bora-like windstorm in western Washington. *Mon. Wea. Rev.,* **109,** 2382–2393.

Reed, T. R., 1931: Gap winds of the strait of Juan de Fuca. *Mon. Wea. Rev.,* **59,** 373–376.

Saito, K., 1992: Shallow water flow having a lee hydraulic jump over a mountain range in a channel of variable width. *J. Meteor. Soc. Japan,* **70,** 775–782.

——, 1993: A numerical study of the local downslope wind ''Yamaji-kaze'' in Japan. Part 2: Non-linear aspect of the 3-D flow over a mountain range with a col. *J. Meteor. Soc. Japan,* **71,** 247–271.

Samelson, R. M., 1992: Supercritical marine-layer flow along a smoothly varying coastline. *J. Atmos. Sci.,* **49,** 1571–1584.

——, and S. J. Lentz, 1994: The horizontal momentum balance in the marine atmospheric boundary layer during CODE-2. *J. Atmos. Sci.,* **51,** 3745–3757.

Schär, C., 1993: A generalization of Bernoulli's theorem. *J. Atmos. Sci.,* **50,** 1437–1443.

——, and R. B. Smith, 1993a: Shallow-water flow past isolated topography. Part I: Vorticity production and wake formation. *J. Atmos. Sci.,* **50,** 1373–1400.

——, and ——, 1993b: Shallow-water flow past isolated topography. Part II: Transition to vortex shedding. *J. Atmos. Sci.,* **50,** 1401–1412.

——, and P. K. Smolarkiewicz, 1996: A synchronous and iterative flux-correction formalism for coupled transport equations. *J. Comput. Phys.,* **128,** 101–120.

——, and D. R. Durran, 1997: Vortex formation and shedding in continuously stratified flows past isolated topography. *J. Atmos. Sci.,* **54,** 534–555.

Scorer, R. S., 1952: Mountain-gap winds: A study of surface wind at Gibraltar. *Quart. J. Roy. Meteor. Soc.,* **78,** 53–61.

Shuchman, R. A., J. A. Johannessen, C. Rufenack, K. Davidson, and C. Wackerman, 1993: Determination of wind speed, wind direction and atmospheric structure using *ERS-1* SAR data during NORCSEX'91. *Proc. 1993 Int. Geoscience and Remote Sensing Symp.,* Institute of Electrical and Electronic Engineers (IEEE), 537–539.

Sikora, T. D., G. S. Young, R. C. Beal, and J. B. Edson, 1995: Use of *ERS-1* synthetic aperture radar imagery of the sea surface in detecting the presence and structure of the convective marine atmospheric boundary layer. *Mon. Wea. Rev.,* **123,** 3623–3632.

Smith, R. B., 1980: Linear theory of stratified hydrostatic flow past an isolated mountain. *Tellus,* **32,** 348–364.

——, 1987: Aerial observations of the Yugoslavian bora. *J. Atmos. Sci.,* **44,** 269–297.

——, 1989: Hydrostatic flow over mountains. *Advances in Geophysics,* Vol. 31, Academic Press, 1–41.

——, and V. Grubišić, 1993: Aerial observations of Hawaii's wake. *J. Atmos. Sci.,* **50,** 3728–3750.

——, and D. F. Smith, 1995: Pseudoinviscid wake formation by mountains in shallow-water flow with a drifting vortex. *J. Atmos. Sci.,* **52,** 436–453.

——, A. C. Gleason, P. A. Gluhosky, and V. Grubisic', 1997: The wake of St.Vincent. *J. Atmos. Sci.,* **54,** 606–623.

Smolarkiewicz, P. K., and R. Rotunno, 1989: Low Froude number flow past three-dimensional obstacles. Part 1: Baroclinically generated lee vortices. *J. Atmos. Sci.,* **46,** 1154–1164.

Stumpf, H. G., 1975: Satellite detection of upwelling in the Gulf of Tehuantepec, Mexico. *J. Phys. Oceanogr.,* **5,** 383–388.

Thomson, R. E., J. F. R. Gower, and N. W. Bowker, 1977: Vortex streets in the wake of the Aleutian Islands. *Mon. Wea. Rev.,* **105,** 873–884

——, P. W. Vachon, and G. A. Borstad, 1992: Airborne synthetic aperture radar imagery of atmospheric gravity waves. *J. Geophys. Res.,* **97,** 14 249–14 257.

Vachon, P. W., O. M. Johannessen, and J. A. Johannessen, 1994: An *ERS-1* synthetic aperture radar image of atmospheric lee waves. *J. Geophys. Res.,* **99,** 22 483–22 490.

——, ——, and D. P. Browne, 1995: *ERS-1* SAR images of atmospheric gravity waves. *IEEE Trans. Geosci. Remote Sens.,* **33,** 1014–1025.